HHS Public Access

Author manuscript

J Am Chem Soc. Author manuscript; available in PMC 2018 October 14.

Published in final edited form as:

J Am Chem Soc. 2018 September 19; 140(37): 11800–11810. doi:10.1021/jacs.8b07362.

Nitric Oxide Modulates Endonuclease III Redox Activity by a 800 mV Negative Shift upon [Fe_4S_4] Cluster Nitrosylation

Levi A. Ekanger[†], **Paul H. Oyala**[†], **Annie Moradian**[†], **Michael J. Sweredoski**[‡], and **Jacqueline K. Barton**[*,†]

[†]Division of Chemistry and Chemical Engineering, Beckman Institute, California Institute of Technology, Pasadena, California 91125, United States

[‡]Proteome Exploration Laboratory, Beckman Institute, California Institute of Technology, Pasadena, California 91125, United States

Abstract

Here we characterize the [Fe_4S_4] cluster nitrosylation of a DNA repair enzyme, endonuclease III (EndoIII), using DNA-modified gold electrochemistry and protein film voltammetry, electrophoretic mobility shift assays, mass spectrometry of whole and trypsin-digested protein, and a variety of spectroscopies. Exposure of EndoIII to nitric oxide under anaerobic conditions transforms the [Fe_4S_4] cluster into a dinitrosyl iron complex, [$(Cys)_2$ $Fe(NO)_2$]-, and Roussin's red ester, [$(\mu$-$Cys)_2Fe_2(NO)_4$], in a 1:1 ratio with an average retention of 3.05 ± 0.01 Fe per nitrosylated cluster. The formation of the dinitrosyl iron complex is consistent with previous reports, but the Roussin's red ester is an unreported product of EndoIII nitrosylation. Hyperfine sublevel correlation (HYSCORE) pulse EPR spectroscopy detects two distinct classes of NO with ^{14}N hyperfine couplings consistent with the dinitrosyl iron complex and reduced Roussin's red ester. Whole-protein mass spectrometry of EndoIII nitrosylated with ^{14}NO and ^{15}NO support the assignment of a protein-bound [$(\mu$-$Cys)_2Fe_2(NO)_4$] Roussin's red ester. The $[Fe_4S_4]^{2+/3+}$ redox couple of DNA-bound EndoIII is observable using DNA-modified gold electrochemistry, but nitrosylated EndoIII does not display observable redox activity using DNA electrochemistry on gold despite having a similar DNA-binding affinity as the native protein. However, direct electrochemistry of protein films on graphite reveals the reduction potential of native and nitrosylated EndoIII to be 127 ± 6 and −674 ± 8 mV vs NHE, respectively, corresponding to a shift of approximately −800 mV with cluster nitrosylation. Collectively, these data demonstrate that DNA-bound redox activity, and by extension DNA-mediated charge transport, is modulated by [Fe_4S_4] cluster nitrosylation.

[*]**Corresponding Author**: jkbarton@caltech.edu.

Supporting Information

The Supporting Information is available free of charge on the ACS Publications website at DOI: 10.1021/jacs.8b07362.

UV−vis spectroscopy of nitrosylation with and without dsDNA, CW and electron-spin echo EPR spectroscopy, representative UV−vis spectra of deoxymyoglobin experiments, UV−vis spectroscopy of nitrosylation using 14/15NO, Q-band HYSCORE spectroscopy and simulations of EndoIII nitrosylated using 14/15NO, trypsin-digested native and nitrosylated EndoIII, representative gels from electrophoretic mobility shift assays, wide-potential sweep on DNA-modified gold electrodes (PDF)

Notes

Theauthors declare no competing financial interest.

Graphical Abstract

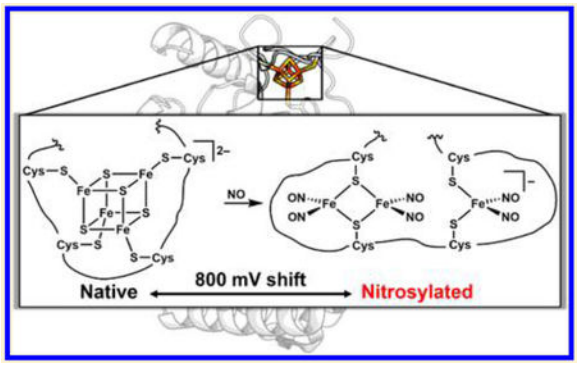

INTRODUCTION

Nitric oxide (NO) is an endogenous reactive nitrogen species that plays an important role in homeostatic regulation,[1–3] cytoprotective and cytotoxic pathways,[4–6] tumor progression,[7–10] and biofilm dispersal.[11] NO often elicits a response by coordinating metal centers of metalloenzymes, such as in heme nitrosylation of soluble guanylyl cyclase during vasodilation.[12] Non-heme Fe centers are also prone to nitrosylation. For example, the transcription factors SoxR, NsrR, and FNR each contain a $[Fe_2S_2]$ or $[Fe_4S_4]$ cluster that react with NO.[13–17] The $[Fe_4S_4]$ clusters in transcription factors often play a functional role by modulating protein conformation which, in turn, modulates DNA-binding affinity and gene expression.[17] Nitrosylation of iron−sulfur clusters typically results in protein-bound iron nitrosyl species such as the relatively common dinitrosyl iron complex, $[(Cys)_2Fe(NO)_2]^-$.[18–20] However, there is growing evidence that other iron nitrosyl species, such as the Roussin's red ester, $[(\mu\text{-}Cys)_2Fe_2(NO)_4]$, a structural analogue of the red iron nitrosyl salt reported by Roussin in 1858 (Figure 1),[21] are more common than previously thought.[22–26] While recent studies have focused on the nitrosylation of transcription factors, the $[Fe_4S_4]$ clusters of DNA repair enzymes, such as endonuclease III (EndoIII) and DinG, are also targets for NO reactivity.[27,28]

The $[Fe_4S_4]$ clusters in DNA repair enzymes were once thought to be strictly structural motifs based on their relatively positive reduction potential. However, upon binding DNA, the close proximity of the polyanionic phosphate backbone negatively shifts the $[Fe_4S_4]^{2+/3+}$ midpoint potential to approximately 80 mV vs normal hydrogen electrode (NHE), thereby activating its redox activity in the DNA-bound form.[29–31] Our laboratory has proposed that redox signaling between DNA-bound $[Fe_4S_4]^{2+}$ and $[Fe_4S_4]^{3+}$ clusters, utilizing DNA-mediated charge transport (DNA CT), facilitates efficient DNA lesion detection.[32] Given the importance of $[Fe_4S_4]$ clusters for DNA CT in biology and their propensity to react with NO, we are interested in studying how NO affects DNA CT by cluster nitrosylation.

Our laboratory has explored DNA CT using EndoIII in *Escherichia coli* as a model $[Fe_4S_4]$ cluster DNA repair enzyme. The $[Fe_4S_4]$ cluster of EndoIII reacts with NO, leading to inactivation of DNA repair.[27] However, $[Fe_4S_4]$ cluster nitrosylation of EndoIII has not been

explored within the context of DNA CT. Here we report the effect of EndoIII [Fe_4S_4] cluster nitrosylation on DNA CT using DNA-modified gold electrochemistry, protein film voltammetry, electro-phoretic mobility shift assays, mass spectrometry of whole and trypsin-digested protein, and UV−vis, continuous-wave (CW) and pulse electron paramagnetic resonance (EPR), and circular dichroism spectroscopies. We connect our biophysical observations within the DNA CT model to account for the electrochemical consequences of [Fe_4S_4] cluster nitrosylation.

EXPERIMENTAL SECTION

General Procedures

All chemicals were of reagent-grade purity or better, purchased from Sigma-Aldrich unless otherwise noted, and used as received unless otherwise noted. Water was purified on a Milli-Q Reference Ultrapure Water Purification System (≥18.2 MΩ cm). Anaerobic atmospheres (3–4% H_2 in N_2, ≤1 ppm of O_2) were maintained in vinyl chambers using Pd scrubbing towers (Coy Laboratories).

EndoIII Overexpression and Purification.

Following reported procedures,[30] *E. coli* EndoIII was overexpressed in BL21star-(DE3)pLysS cells containing a pET11-His_6-ubiquitin-*nth* construct. Purification was performed at 4 °C using fast protein liquid chromatography (Bio-Rad). Protein was kept in storage buffer (20 mM phosphates, 150 mM NaCl, 0.5 mM EDTA, 10% v/v glycerol, pH 7.5) at −80 °C until further use. Purity of isolated EndoIII was ≥95% as determined by SDS-PAGE. EndoIII concentrations were determined by UV−vis using peptide and [Fe_4S_4] cluster absorbances at 280 ($\varepsilon = 19.94 \times 10^3\ M^{-1}\ cm^{-1}$ as calculated by ExPASy ProtParam, Swiss Institute of Bioinformatics) and 410 nm ($\varepsilon = 17.0 \times 10^3\ M^{-1}\ cm^{-1}$),[33] respectively.

EndoIII Nitrosylation with Natural Abundance NO.

NO was introduced to reaction solutions through the proton-mediated decomposition of 1-(hydroxy-NNO-azoxy)-L-proline, disodium salt (PROLI NONOate, Cayman Chemicals). PROLI NONOate (~10 mg aliquot in vial) was dissolved in 400 μL of a solution of Ar-sparged NaOH (0.01 M), quantified by UV−vis absorbance at 252 nm ($\varepsilon = 8.40 \times 10^3\ M^{-1}\ cm^{-1}$),[34] and stored on ice under an anaerobic atmosphere until further use. EndoIII nitrosylation reactions were prepared by bringing an aliquot of EndoIII (100 μM in storage buffer) on ice into the anaerobic chamber. Within the anaerobic chamber, PROLI NONOate (typically 80–85 mM in 0.01 M NaOH) was added directly to Ar-sparged storage buffer (pH 7.5) to initiate the decomposition of PROLI NONOate (3.75 mM), which was vortexed and used within 5 min of preparation. PROLI NONOate in buffer was mixed with an appropriate volume of storage buffer and EndoIII to achieve a 1:50 EndoIII/NO ratio (1 equiv of PROLI NONOate decomposes to 2 equiv of NO). The final concentration of EndoIII was 60 μM during nitrosylation in a total reaction volume of 83 μL. After 10 min and still within the anaerobic chamber, the nitrosylation reaction solution was loaded onto a pre-rinsed Micro Bio-Spin 6 size-exclusion column (Bio-Rad) and spun into a clean 1.5 mL tube following the manufacturer's protocol. For every nitrosylation reaction, a non-NO-exposed control was

included and also purified by a size-exclusion column. Experiments and successive dilutions or concentrations were performed using filtrate collected after size-exclusion purification.

UV−Vis, Circular Dichroism, and CW EPR Spectroscopies.

UV−vis data were acquired using either a Cary 100 Bio (Agilent) or DeNovix DS-C spectrophotometer. Circular dichroism spectroscopy was performed using an AVIV Biomedical spectrometer in the Beckman Institute Laser Resource Center. In an anaerobic chamber, protein collected from size-exclusion purification was diluted to 10 μM in a total volume of 800 μL and loaded into rectangular spectrophotometer cells with 2 mm path length (Starna Cells). Spectra are normalized to ellipticity minima at 222 nm.

X-band CW-EPR spectroscopy was performed on an EMX X-band spectrometer (Bruker) equipped with an ESR-900 cryogen flow cryostat (Oxford) and an ITC-503 temperature controller. Samples (150 μL each) were loaded into 4 mm thin-wall precision quartz EPR tubes (Wilmad LabGlass, 715-PW-250MM). To reduce dinitrosyl iron and Roussin's red complexes, nitrosylated EndoIII was incubated with sodium dithionite (1:25 protein/dithionite ratio) for 30 min prior to freezing in liquid nitrogen while remaining capped under an anaerobic atmosphere. An acquisition temperature of 60 K and microwave power of 0.204 mW were used for the ratiometric comparison of double integration spin intensities because the iron nitrosyl signals were not saturated under these conditions. Signal saturation was evaluated by ensuring signal intensity grew as the square root of microwave power. Double integration spin intensities were measured using Matlab R2016a.

Synthesis of ^{15}NO and Quantification with Deoxymyoglobin.

To a 10 mL conical tube was added $Na^{15}NO_2$ (400 mg, 5.72 mmol, 98 atom % ^{15}N) and $FeSO_4{\cdot}7H_2O$ (2.00 g, 7.19 mmol). The tube was capped with a rubber septum and charged with Ar. The dropwise addition of concentrated H_2SO_4 (4 mL) into the capped reaction vessel produced heat and vigorous gas evolution which was directed by cannula from the reaction vessel into the bottom of a NaOH scrubbing tower (10 mL, 1 M). Gases from the headspace of the scrubbing tower were further directed by a separate cannula and bubbled into a 4 mL glass vial containing 2 mL of ice-cold degassed buffer (20 mM phosphates, 150 mM NaCl, 0.5 mM EDTA, 10% v/v glycerol, pH 7.5). At the time of bubbling, the glass vial was capped with a rubber septum, and a needle was used as a vent to relieve pressure in the system. After gas evolution from the reaction vessel had ceased (2–3 min of gas bubbling), the glass vial with buffer was brought into an anaerobic chamber remaining capped and on ice. The concentration of ^{15}NO in the buffer was determined under an anaerobic atmosphere using a deoxymyoglobin colorimetric method.

The method for determining the concentration of dissolved NO in buffer is adapted from a reported procedure.[35] Equine heart metmyoglobin (27 mg, 1.53 μmol) was dissolved in 500 μL buffer (20 mM phosphates, 150 mM NaCl, 0.5 mM EDTA, 10% v/v glycerol, pH 7.5) and reduced to deoxymyoglobin using sodium dithionite (7.6 mg, 43.7 μmol) under an anaerobic atmosphere. Excess sodium dithionite was removed by size-exclusion purification using Micro Bio-Spin 6 size-exclusion columns (Bio-Rad). The reduction of metmyoglobin to deoxymyoglobin is evidenced by a shift in the Soret band from 418 nm for metmyoglobin

to 434 nm for deoxymyoglobin. The UV−vis spectrum of deoxymyoglobin indicates no observable contamination by oxymyoglobin (418, 542, and 580 nm) or metmyoglobin (408, 502, and 630 nm). The concentration of deoxymyoglobin was 3.62 mM determined using a reported extinction coefficient of 114 mM^{-1} cm^{-1} at 434 nm.[35,36]

Deoxymyoglobin was used to quantify the concentration of ^{15}NO dissolved in buffer by a ratiometric comparison with ^{14}NO. PROLI NONOate was used to prepare a solution of ^{14}NO with excess deoxymyoglobin (^{14}NO/deoxymyoglobin ratio of 1:1.3). A separate solution was prepared at the same time containing an aliquot of ^{15}NO solution added to the same quantity of deoxymyoglobin used for the ^{14}NO standard. After 1 h of equilibration under an anaerobic atmosphere, UV−vis absorbances at 420 nm were used to calculate the concentration of the 15NO solution based on the known concentration of ^{14}NO using eq 1.

$$\left[{}^{15}\mathrm{NO}\right] = \left({}^{15\mathrm{NO}}A_{420}/{}^{14\mathrm{NO}}A_{420}\right)\left[{}^{14}\mathrm{NO}\right] \quad (1)$$

EndoIII Nitrosylation with ^{15}NO.

A 33.3 μL aliquot of ^{15}NO (2.7 mM) in ice-cold buffer was added to EndoIII under an anaerobic atmosphere. After 10 min, the reaction solution was purified by size-exclusion purification on pre-rinsed Micro Bio-Spin 6 size-exclusion columns (Bio-Rad). Experiments and successive dilutions or concentrations were performed using filtrate collected after size-exclusion purification.

Pulse EPR.

Samples for hyperfine sublevel correlation (HYS-CORE) EPR spectroscopy were prepared by concentrating nitrosylated EndoIII samples with or without dithionite treatment using Amicon Ultra Centrifugal Filters (10k molecular weight cut off) to a concentration of 0.5 mM protein in 75 μL.

All pulse X-band (9.7 GHz) and Q-band (34 GHz) EPR and HYSCORE spectroscopy was performed using a Bruker ELEXSYS E580 pulse EPR spectrometer equipped with a Bruker MD4 (X-band) or D2 (Q-band) resonator. Temperature control was achieved using an ER 4118HV-CF5-L Flexline Cryogen-Free VT cryostat manufactured by ColdEdge equipped with an Oxford Instruments Mercury ITC temperature controller.

Pulse X- and Q-band HYSCORE spectra were acquired using the 4-pulse sequence ($\pi/2 - \tau - \pi/2 - t_1 - \pi - t_2 - \pi/2 - \tau -$ echo), where τ is a fixed delay, and t_1 and t_2 are variable delays independently incremented by Δt_1 and Δt_2, respectively. Sixteen step phase cycling was utilized to eliminate contributions from secondary/tertiary echoes. The time domain spectra were baseline-corrected (third-order polynomial), apodized with a Hamming window function, zero-filled to 8-fold points, and fast Fourier-transformed to yield the frequency domain.

All EPR spectra (CW, HYSCORE) were simulated using the EasySpin[37] simulation toolbox (version 5.2.16) with Matlab 2016b (see SI for description of simulations).

Ferene Assay for Fe Quantitation.

The ferene assay was performed according to a published protocol.[38] Briefly, samples were diluted 1:1 with HNO_3 (21.7% v/v) to a total volume of 200 μL. Samples were heated at 95 °C for 30 min, cooled at 4 °C for 10 min, and centrifuged. To each sample was added 600 μL of ammonium acetate (7.5% w/v), 100 μL of ascorbic acid (12.5% w/v), and 100 μL of 3-(2-pyridyl)-5,6-di(2-furyl)-1,2,4-triazine-5′,5′′,-disulfonate (ferene, 10 mM). Samples were incubated under ambient conditions for 30 min before absorbance at 593 nm was recorded. Calibration curves were prepared using Fe standard solution (1001 ± 2 mg/L Fe in 2% v/v HNO_3, TraceCERT Fe standard for ICP).

Protein Mass Spectrometry.

Whole protein was analyzed using an Agilent 1100 series liquid chromatography mass selective detector (LC/MSD) system. Following size-exclusion purification, control and nitrosylated protein samples were diluted 1:50 or 1:20 in formic acid (0.2% v/v), respectively. Trypsin-digested protein samples were prepared by adding 5 μL of protein solution (60 μM) to 45 μL of sodium deoxycholate (1% w/v) in Tris buffer (100 mM, pH 8.5). Disulfides were reduced by adding 0.5 μL of tris(2-carboxyethyl)-phosphine (TCEP, 0.5 M in water) and, after 20 min, protected by adding 1 μL of iodoacetamide (0.5 M in water) followed by 20 min incubation in the dark under ambient conditions. To preserve disulfide bonds in some samples, TCEP was omitted from the digestion protocol. After thiol protection, 1 μL of lysyl endopeptidase (0.1 μg/μL in 100 mM Tris buffer, pH 8.5) was added to protein samples. After incubating for 2.5 h under ambient, dark conditions, all samples were diluted by half with the addition of Tris buffer (100 mM, pH 8.5) followed by the addition of 1 μL $CaCl_2$ (100 mM in water) and 1 μL trypsin (0.44 μg/μL in 100 mM Tris buffer, pH 8.5). After digesting overnight at 37 °C, samples received formic acid (5% v/v) to bring the total sample volume to 95 μL and produce a cloudy, white precipitate which was removed by centrifugation. Purification of the supernatant was performed by reverse-phase high-performance liquid chromatography (HPLC), and solvent removed from purified samples by vacuum centrifugation. Dried samples were dissolved in formic acid (0.2% v/v) and were injected onto a capillary in-house packed C18 column and subjected to a 60 min gradient by an Easy nLC 1200 HPLC. Chromatographically separated peptides were analyzed using a Q Exactive mass spectrometer (ThermoScientific) coupled to a NanoFlex ion source.

Synthesis and Characterization of Thiol-Modified DNA.

All oligonucleotides were purified by reverse-phase HPLC using a C-18 column (Agilent). Disulfide-modified oligonucleotide was synthesized on a 3400 Applied Biosystems DNA synthesizer using standard phosphoramidite chemistry (all phosphoramidites were purchased from Glen Research), where the C6 S−S phosphoramidite was installed at the 5′ terminus. Disulfide-modified oligonucleotide was cleaved from the solid support, purified by HPLC, and reduced to hexanethiol-modified oligonucleotide (5′ HS-C_6-GTG CTG CAA CGT GTC TGC GC 3′) with dithiothreitol in buffer (50 mM Tris, 50 mM NaCl, pH 8.4). Thiol-

modified oligonucleotide was purified by size-exclusion chromatography (GE Illustra NAP-5 column), HPLC, and characterized by matrix-assisted laser desorption ionization time-of-flight mass spectrometry (MALDI−TOF, Bruker Autoflex); MALDI−TOF (*m/z*): $[M + H]^+$ calculated for $C_{200}H_{264}N_{73}O_{124}P_{20}S$, 6323.1; found, 6323.2. The complementary strand (5′ GCG CAG ACA CGT TGC AC 3′) was purchased from IDT and purified by HPLC. Oligonucleotides were further purified after HPLC by ethanol precipitation. Thiol-modified oligonucleotide was annealed to its complement (50 μM oligonucleotides in Arsparged buffer containing 5 mM sodium phosphates, 50 mM NaCl, pH 7.0) by heating at 90 °C for 5 min followed by cooling to ambient temperature over 90 min. Thiol-modified double-stranded DNA was stored under Ar at −20 °C until further use.

DNA-Modified Gold Electrochemistry.

The fabrication of multiplexed gold chips has been previously described.[39,40] Multiplexed gold chips were cleaned in acetone and isopropanol with sonication, dried under an Ar stream, and ozone-cleaned for 25 min (UVO Cleaner). Immediately after cleaning, a rubber gasket (Buna-N) and acrylic clamp were affixed to the chip surface, and thiol-modified dsDNA (20 μL, 50 μM) was added to each quadrant to form a self-assembled monolayer on the gold electrode surface. After incubation with thiol-modified DNA for 18–21 h, quadrants were washed with buffer (5 mM sodium phosphates, 50 mM NaCl, pH 7.0) and incubated with 6-mercaptohexanol (1 mM in 5 mM sodium phosphates, 50 mM NaCl, pH 7.0). After 45 min, the electrode was washed three times with Ar-sparged storage buffer and brought into the anaerobic chamber for electrochemical analyses. A three-electrode setup was employed consisting of DNA-modified gold working electrodes, Ag/AgCl reference electrode (MW-2030, RE-6, BASi) with a gel tip (1.0% UltraPure Invitrogen Agarose prepared with 3 M NaCl), and a Pt wire auxiliary electrode. The total volume on the multiplexed chip was 200 μL. A scan rate of 100 mV/s was used for cyclic voltammograms, and potentials were converted to the NHE scale.

Direct Electrochemistry on Edge-Plane Graphite.

Protein films were prepared on an edge-plane pyrolytic graphite electrode (Pine Research Instrumentation). Prior to protein deposition, the electrode was cleaned by abrasion on sandpaper (400 grit) followed by sonication in isopropanol then water. Clean surfaces were confirmed by performing electrochemical experiments with protein storage buffer that did not contain glycerol. Micro Bio-Spin (Bio-Rad) columns were used to exchange sample buffer with protein storage buffer that did not contain glycerol to enable dry film formation. Protein films were deposited onto the electrode surface under an anaerobic atmosphere by sequential drying of protein aliquots (3 × 25 μL). Drying was accomplished by placing the upright electrode with aliquot in the airstream of a Pd catalyst fan box equipped with a single catalyst pack (Coy Laboratories) for approximately 20 min per aliquot. Dried protein films were secured with 10 μL Nafion (5% aqueous dispersion) to prevent film dispersal as previously described.[41] After protein and Nafion depositions, a droplet (50 μL) of protein storage buffer without glycerol was added on top of the film. A three-electrode setup was employed by submerging reference and auxiliary electrodes in the droplet. The reference and auxiliary electrodes were the same used for DNA-modified gold electro-chemistry experiments described above. All potentials were converted to the NHE scale.

Electrophoretic Mobility Shift Assays.

A non-thiol-functionalized analogue of the oligonucleotide used for DNA-modified electrochemistry (5′ GTG CTG CAA CGT GTC TGC GC 3′) was purchased from IDT, purified by HPLC and ethanol precipitation, and radiolabeled through 5′ phosphorylation using [γ-^{32}P] ATP (NEG035C005MC, 6000 Ci/mmol, 150 mCi/mL, PerkinElmer) and T4 polynucleotide kinase (New England BioLabs) at 37 °C for 30 min followed by heat inactivation at 65 °C for 20 min. Purification of ^{32}P-labeled oligonucleotide was accomplished by size-exclusion purification through a Micro Bio-Spin 6 column (Bio-Rad) followed by a Monarch PCR & DNA Cleanup Kit (New England BioLabs) with a modified protocol. Briefly, to 50 μL of filtrate from size exclusion were added 100 μL Monarch DNA Cleanup Binding Buffer and 300 μL ethanol. The resulting solution was loaded into a Monarch DNA Cleanup Column and spun at 16,000 × *g* for 1 min. After discarding the flow-through, 500 μL of a 1:4 solution of Monarch DNA Cleanup Binding Buffer and ethanol were added to the column and spun at 16,000 × *g* for 1 min. This washing procedure was repeated once more and flow-through discarded each time. The column was spun at 16,000 × *g* for 1 min to remove residual ethanol, transferred to a clean 1.5 mL tube, and 25 μL of Monarch Elution Buffer was carefully added to the center of the column matrix. After 1 min, the column was spun at 16,000 × *g* for 1 min to collect the purified, radiolabeled oligonucleotide, which was then annealed to its non-radiolabeled complement (10 μM oligonucleotides in buffer containing 5 mM sodium phosphates, 50 mM NaCl, pH 7.0) by heating at 90 °C for 10 min followed by cooling to ambient temperature over 3 h. Complete annealing was verified by native 10% polyacrylamide gel electrophoresis at 4 °C (50 V, 0.5× Tris/borate/EDTA buffer) using single-stranded controls. Gels were imaged by dark exposure to BAS storage phosphor screens followed by imaging on a Typhoon FLA 9000 Imager (GE Healthcare Life Sciences). Radiolabeled dsDNA was incubated with native or nitrosylated EndoIII for 1 h at 4 °C prior to native 10% polyacrylamide gel electrophoresis at 4 °C (50 V for 3 h in 1× TGX buffer). Gel exposure time was calculated by the radioactivity of a 10 μL aliquot where a scintillation reading of 300,000 counts per minute corresponded to 1 h exposure on storage phosphor screens. Free dsDNA band intensity was measured using ImageQuant 5.2, and normalized band intensities were used to calculate dissociation constants by the Hill function in OriginPro 2017.

RESULTS AND DISCUSSION

Characterization of Nitrosylated EndoIII by UV−vis Spectroscopy and the Ferene Assay.

We sought to characterize the products of EndoIII nitrosylation to enable a rational interpretation of our biophysical observations. At the outset of our work, the reaction between NO and the $[Fe_4S_4]^{2+}$ cluster of EndoIII was reported with a focus on the titration of EndoIII with NO, enzyme activity, and the reversibility of $[Fe_4S_4]^{2+}$ cluster nitrosylation.[27] Additionally, the dinitrosyl iron complex, $[(Cys)_2Fe(NO)_2]^-$, was the only protein-bound iron nitrosyl species observed.[27] In the absorbance spectrum of native EndoIII, we observe absorbances at 280 and 410 nm consistent with the presence of a protein-bound $[Fe_4S_4]^{2+}$cluster.[33] The $[Fe_4S_4]^{2+}$ cluster of native EndoIII is relatively stable to handling in air, but NO degrades the cluster within a 10 min reaction period. The absorbance spectrum of nitrosylated EndoIII is similar to native EndoIII at 280 nm but differs at longer

wavelengths primarily through a 46 nm hypsochromic shift of the cluster absorbance maximum to a new feature at 364 nm (Figure 2). This nitrosylation reaction proceeds similarly in the presence of excess dsDNA (EndoIII/dsDNA ratio of 1:10) as evidenced by a nearly identical UV− vis absorbance spectrum (Figure S1). The new absorbance centered at 364 nm is consistent with a Roussin's red ester, $[(\mu\text{-Cys})_2Fe_2(NO)_4]$, which exhibits a highly conserved absorbance maximum in the 360 ± 10 nm range in proteins, peptides, and synthetic model complexes.[22,24,42–45]

Additional support for the presence of a multinuclear iron nitrosyl complex stems from ferene colorimetric assays, which were used to quantify protein-bound Fe of native and nitrosylated EndoIII. The concentration of protein-bound $[Fe_4S_4]$ cluster was determined using the reported extinction coefficient of $17.0 \times 10^3\ M^{-1}\ cm^{-1}$ at 410 nm,[33] and the concentration of Fe per cluster was measured using the ferene colorimetric assay where ferene-chelated Fe(II) is detected at 593 nm (Figure 2). Native EndoIII was found to contain 4.00 ± 0.09 Fe per cluster, and this value decreased to 3.05 ± 0.01 Fe for nitrosylated EndoIII prepared from a 10 min exposure to NO. If $[(Cys)_2Fe(NO)_2]-$ is the only iron nitrosyl species to form in the tetracysteine cluster-binding pocket, then nitrosylated EndoIII should retain only 1 or 2 Fe per nitrosylated cluster. Accordingly, the retention of 3 Fe per nitrosylated cluster strongly indicates that an iron nitrosyl species with more than 1 equiv of Fe is present, which is likely the $[(\mu\text{-Cys})_2Fe_2(NO)_4]$ Roussin's red ester based on UV−vis observations described above. The retention of 3 Fe in nitrosylated EndoIII necessitates the release of 1 Fe equivalent in a labile form which is subsequently removed from our reaction solutions by size-exclusion purification. The release of labile Fe upon reaction with NO is consistent with cluster degradation.[17]

Characterization of Nitrosylated EndoIII by CW EPR Spectroscopy.

To gain further insight into the products of EndoIII nitrosylation, we performed CW and pulse EPR experiments using native and nitrosylated EndoIII in the absence of DNA. The CW EPR spectrum of native EndoIII is devoid of signal and consistent with a diamagnetic sample (Figure S2), while the corresponding spectrum of nitrosylated EndoIII contains a slightly rhombic signal with g = [2.042, 2.036, 2.015], consistent with a mononuclear $[(Cys)_2Fe(NO)_2]^-$ dinitrosyl iron complex (Figure 2).[22,42]

When nitrosylated EndoIII is treated with sodium dithionite (protein/dithionite ratio of 1:25), a new axial signal with $g_\perp$ = 2.011 and $g_\parallel$ = 1.972 emerges consistent with the binuclear $[(\mu\text{-Cys})\ Fe_2\ (NO)_4]^-$ complex referred to as the reduced Roussin's red ester.[22,42] A ratiometric comparison of the double-integration spin intensities indicates that $[(Cys)_2Fe(NO)_2]^-$ and $[(\mu\text{-Cys})_2\ Fe(NO)_4]^-$ form in a 1:1 ratio (see Figures S3 and S4 for comparison of single-integration signals and simulations of CW EPR spectra, respectively).

To simplify electron counting and avoid assigning formal oxidation states in iron nitrosyl complexes, the Enemark− Feltham notation, $\{M(NO)_x\}^n$, is used where M is the metal center, x is the number of metal-bound nitrosyl ligands, and n is the total number of electrons in the metal d and NO π^* orbitals.[46] The CW EPR spectrum of native EndoIII is devoid of any observable signal, consistent with a diamagnetic $[Fe_4S_4]^{2+}$ cluster[47], while nitrosylated EndoIII exhibits a rhombic signal centered at g = 2.029 consistent with the

presence of an $\{Fe(NO)_2\}^9$ dinitrosyl iron complex.[22,42] Interestingly, when nitrosylated EndoIII is reduced with dithionite, the $\{Fe(NO)_2\}^9$ profile diminishes, and a new axial signal is observed with $g_\perp = 2.011$ and $g_\parallel = 1.972$. The $\{Fe(NO)_2\}^9$ dinitrosyl iron complex is the only species observed by EPR directly after cluster nitrosylation because it is the only paramagnetic ($S = 1/2$) species initially formed, while the $\{Fe(NO)_2\}^9$–$\{Fe(NO)_2\}^9$ Roussin's red ester, a dimerized analogue of the dinitrosyl iron complex, contains two antiferromagnetically coupled Fe centers and is therefore EPR silent as synthesized. Upon reduction by dithionite, the $\{Fe(NO)_2\}^9$ dinitrosyl iron complex is reduced into an EPR-silent $\{Fe(NO)_2\}^{10}$ complex, while the EPR-silent $\{Fe\text{-}(NO)_2\}^9$–$\{Fe(NO)_2\}^9$ Roussin's red ester is reduced into the EPR-active $\{Fe(NO)_2\}^9$–$\{Fe(NO)_2\}^{10}$ ($S = 1/2$) species referred to as the reduced Roussin's red ester (Scheme 1).[22,43] Our assignment of the reduced Roussin's red ester, $[(\mu\text{-Cys})_2Fe_2(NO)_4]^-$, is supported by similar EPR resonances observed for synthetic and peptide-bound model complexes.[23,42,48]

It should be noted that the reduced Roussin's red ester signal with principal g-values of $g_\perp = 2.011$ and $g_\parallel = 1.972$ was originally assigned as a d^9 dinitrosyl iron complex having been reduced from a d^7 form.[19] However, compelling spectroscopic data of structurally well-characterized model complexes disagree with the initial assignment and instead support the assignment of a reduced Roussin's red ester.[42,45] The spectroscopic agreement between reduced Roussin's red ester model complexes and other protein-bound iron nitrosyl species, once considered d^9 dinitrosyl iron complexes, has been noted previously.[23] It therefore appears the protein-bound Roussin's red ester, once overlooked due to its EPR-silent nature in the neutral form, is indeed more common than previously thought.[22–26]

Collectively, these CW EPR data support the observation that nitrosylated EndoIII contains both the dinitrosyl iron complex and Roussin's red ester. The reason that the Roussin's red ester has not been explicitly reported for EndoIII is likely because it is EPR silent. To measure the ratio of dinitrosyl iron complex to reduced Roussin's red ester, the CW EPR signals were compared. The doubly integrated spectral intensities of $\{Fe(NO)_2\}^9$ and $Fe(NO)_2\}^9$–$\{Fe(NO)_2\}^{10}$ reveal they form in a 1:1 ratio, indicating EndoIII retains 1 Fe equivalent from $[(Cys)_2\ Fe(NO)_2]^-$ and 2 Fe equivalents from $[(\mu\text{-Cys})_2Fe_2(NO)_4]$ for a total retention of 3 Fe per nitrosylated cluster. This observation is consistent with the ferene assay results where nitrosylated EndoIII retains an average of 3.05 ±0.01 Fe per nitrosylated cluster. Considering the $[Fe_4S_4]^{2+}$cluster is bound by four cysteine residues, and that dinitrosyl iron complex and Roussin's red ester each require only two cysteine residues, it is likely that the cysteine residues originally bound to the $[Fe_4S_4]$ cluster are responsible for binding the iron nitrosyl species after nitrosylation.

Characterization of Nitrosylated EndoIII by Pulse-EPR Spectroscopy with $^{14/15}$NO.

To gain further insight into the electronic structure of protein-bound iron nitrosyl complexes through measurement of the nitrosyl $^{14/15}$N hyperfine interactions, we performed pulse EPR experiments. Initial characterization by X-band HYSCORE spectroscopy of $[(Cys)_2Fe(NO)_2]^-$ and $[(\mu\text{-Cys})_2Fe_2(NO)_4]^-$ prepared using natural abundance (^{14}N = 99.63%) NO reveals features consistent with two distinct classes of hyperfine couplings from ^{14}N nuclei of the nitrosyl ligands (Figure 3), with one relatively weakly coupled ^{14}N

exhibiting signals in the (+,+) quadrant and a more strongly coupled ^{14}N exhibiting features in the (−,+) quadrant (Figure 3).

In order to further confirm these assignments and constrain the hyperfine coupling and nuclear quadrupole interaction parameters independently, Q-band (34 GHz) HYSCORE spectroscopy was performed on samples generated with isotopically enriched ^{15}N (I = 1/2), generated from $^{15}NO^{-}_{2}$ and quantified using deoxymyoglobin (see Figures S5 and S6 for representative UV−vis spectra), and natural abundance NO (Figure 4). The Q-band HYSCORE spectra of the ^{15}NO isotopologues of both the of $[(Cys)_2Fe(NO)_2]^{-}$ and $[(\mu\text{-}Cys)_2Fe_2(NO)_4]^{-}$ differ markedly from their natural abundance variants, confirming that these features indeed arise from hyperfine couplings to the NO nitrogens. Elimination of nuclear quadrupole interactions in the ^{15}NO samples allowed for the 15N hyperfine couplings to be determined via simulation (see Figures S7−S9 for Q-band HYSCORE spectra and simulations of ^{14}N/^{15}N hyperfine couplings). Accounting for the ratio of $^{15/14}$N nuclear g-values (^{15}N g_n/^{14}N g_n =−1.403), the ^{14}N hyperfine couplings were then fixed (Table 1), and the nuclear quadrupole coupling constant (e^2qQ/h) and electric field gradient asymmetry (η) determined for each ^{14}N nucleus via simulation of the data.

Simulations of the combined multifrequency HYSCORE data set for the EndoIII $[(Cys)_2Fe(NO)_2]^{-}$ dinitrosyl iron complex indicate nitrogen hyperfine couplings to two distinct classes of NO, one more strongly coupled with ^{14}N a_{iso} = 9.5 MHz and the other much more weakly coupled with ^{14}N a_{iso} = 0.4 MHz. The non-equivalence the two NO ligands is expected because dinitrosyl iron species exhibit two distinct NO stretching frequencies.[35] This non-equivalence is also predicted by density functional theory.[49] These relatively small 14N hyperfine couplings are consistent with the assignment of an $\{Fe(NO)_2\}^9$ dinitrosyl iron complex with spin density largely localized on the Fe center as opposed to an $\{Fe(NO)\}^7$ species, which exhibit much larger ^{14}N hyperfine couplings ($a_{iso} \geq$ 30 MHz, up to 220 MHz) due to unpaired spin being primarily localized on the NO moiety.[35]

Similarly, the multifrequency HYSCORE data set for the EndoIII $[(\mu\text{-}Cys)_2\ Fe_2(NO)_4]^{-}$ reduced Roussin's red ester also indicates nitrogen hyperfine couplings to two distinct classes of NO, one more strongly coupled with ^{14}N a_{iso} = 3.9 MHz and the other more weakly coupled with ^{14}N a_{iso} = 1.9 MHz. Because this species consists of a mixed-valence, antiferromagnetically coupled $\{Fe(NO)_2\}^9$ −$\{Fe(NO)_2\}^{10}$ (S = 1/2) dimer, these two classes of NO ^{14}N hyperfine couplings likely represent two non-equivalent NO ligands on the $\{Fe(NO)_2\}^9$ fragment (analogous to the dinitrosyl iron complex) with no significant contribution from the NO ligands on the diamagnetic $\{Fe(NO)_2\}^{10}$ fragment.

Collectively, the relatively low magnitude of the ^{14}N nuclear quadrupole coupling constants observed for all of the NO nitrogens, e^2qQ/h = 0.8–1.4 MHz combined with the low estimation for the electric field gradient asymmetry (η) indicate axial symmetry of charge about the NO nitrogen with significant population of charge density in the NO π orbitals orthogonal to the NO σ orbital, as expected for the multiply bonded NO moiety (see Table 1 for specific simulation parameters).

In sum, these HYSCORE data further demonstrate that the dinitrosyl iron complex and Roussin's red ester are both products of $[Fe_4S_4]^{2+}$ cluster nitrosylation in EndoIII.

Mass Spectrometry of Native and Nitrosylated EndoIII

Having identified and characterized iron nitrosyl complexes through UV−vis and EPR spectroscopies, we turned to mass spectrometry for further characterization of protein-bound iron nitrosyl species. Whole protein was analyzed by diluting native and nitrosylated EndoIII in formic acid (0.2% v/v) followed by HPLC−MS. Native EndoIII has a lone mass at 33,264 Da corresponding to apoprotein where the cysteines originally binding the cluster are instead protonated (Figure 4). This observation indicates the EndoIII $[Fe_4S_4]$ is acid labile. Nitrosylated EndoIII yields multiple masses of relatively high abundance that provide insight into nitrosylation reaction products. First, masses at 33,260 and 33,292 Da correspond to apoprotein with two cysteine disulfides (2 Cys-SS-Cys) and apoprotein with one cysteine disulfide and one cysteine trisulfide (Cys-SS-Cys + Cys-SSS-Cys), respectively. Disulfide formation and the retention of cluster sulfides as polysulfides of cysteine are common features of $[Fe_4S_4]$ cluster degradation by both NO and O_2.[17] In addition to apoprotein masses, we observe a mass at 33,494 Da corresponding to protein-bound $[(\mu\text{-Cys})_2Fe_2(NO)_4]$ present with a cysteine disulfide (33,264 −2 + 232). To test whether the mass at 33,494 Da arises from protein-bound $[(\mu\text{-Cys})_2Fe_2(NO)_4]$, we performed additional whole-protein mass spectrometry on nitrosylated EndoIII prepared using ^{15}NO and observe a new mass at 33,498 Da (Figure 4). This 4 Da mass shift is consistent with the substitution of four ^{14}NO ligands for ^{15}NO and therefore supports the assignment of 33,494 Da as protein-bound $[(\mu\text{-Cys})_2Fe_2(NO)_4]$. The ^{15}N-enriched sample displays a 4 Da mass shift because only the Roussin's red ester is present in EndoIII after dilution in acid. This can be rationalized considering that the pK_a of bridging cysteine thiolates of the Roussin's red ester should be lower than the pK_a of non-bridging thiolates of the dinitrosyl iron complex, rendering the dinitrosyl iron complex more acid labile than the Roussin's red ester. These observations are similar to a recent report on the mass spectrometric detection of protein-bound Roussin's red ester of the transcription factor NsrR.[50]

We next turned to mass spectrometry of trypsin-digested protein to test for specific off-target modifications to EndoIII caused by NO exposure. By itself, NO has selective reactivity for metal centers and thiols, but does not react directly with other amino acids. However, direct amino acid modification, commonly in the form of tyrosine nitration, can occur in the presence of NO_2 formed from the reaction between NO and O_2.[51] For this reason, the nitrosylation reactions performed in this work were performed under anaerobic conditions. However, we still tested whether tyrosine nitration of EndoIII occurs specifically from NO treatment from the presence of residual O_2 in reaction solutions. To test for tyrosine nitration specific to NO treatment, we digested native and nitrosylated EndoIII with trypsin, and the resulting peptides were analyzed by electron-transfer dissociation mass spectrometry. While we detect peptides modified by tyrosine nitration, the modification does not appear specific to NO exposure (Figure S10) thereby indicating minimal off-target effects.

Cluster Nitrosylation Abates DNA-Bound Redox Activity of EndoIII.

DNA-bound redox activity is a hallmark of DNA-processing proteins that participate in DNA CT. The DNA-bound redox activity of $[Fe_4S_4]$ cluster proteins is typically evaluated using DNA-modified gold electrodes, where the $[Fe_4S_4]^{2+/3+}$ redox couple of the DNA-bound protein is observed near a midpoint potential of 80 mV vs NHE.[29–32] Because the current at 80 mV vs NHE reflects redox activity of the DNA-bound $[Fe_4S_4]$ cluster protein, signal intensity at 80 mV vs NHE reflects the ability of a protein to participate in DNA CT. We observe DNA-bound redox activity of native EndoIII at 80 mV vs NHE purified by size-exclusion filtration (Figure 5). However, no redox activity above the buffer background is observed on the same DNA-modified electrode for nitrosylated EndoIII purified by size-exclusion filtration.[52] The absence of DNA-bound redox activity can be explained by either of the following two factors: (1) The DNA-binding affinity of nitrosylated EndoIII is lower than that of native EndoIII, or (2) the reduction potential of nitrosylated EndoIII is no longer at 80 mV vs NHE and is shifted out of the potential window for the DNA-modified gold electrode. In both of these scenarios, the redox activity at 80 mV vs NHE would decrease for nitrosylated EndoIII relative to the native enzyme. To examine these hypotheses in more detail, we turned to DNA-binding affinity measurements.

Native and Nitrosylated EndoIII Have Different Conformations but Similar DNA-Binding Affinities.

One explanation for the lack of observable redox activity with nitrosylated EndoIII on DNA-modified gold electrodes is that nitrosylated EndoIII binds DNA with a lower affinity than native EndoIII. We therefore examined changes to EndoIII DNA-binding affinity caused by $[Fe_4S_4]$ cluster nitrosylation. To test if nitrosylated EndoIII has a lower DNA-binding affinity than native EndoIII, we performed electrophoretic mobility shift assays. The assays were performed by incubating native and nitrosylated EndoIII with radiolabeled dsDNA followed by native gel electrophoresis. The percentage of EndoIII-bound dsDNA was visualized by phosphoimagery (see representative gels in Figure S11), quantified by measuring band intensities, and used to calculate dissociation constants with Hill function fitting (Figure 5). Through these assays, native and nitrosylated EndoIII show similar DNA dissociation constants of 3.7 ± 0.4 and 2.2 ± 0.1 μM, respectively. If anything, the DNA affinity for the nitrosylated protein is higher, as would be expected given the more positive charge on the cluster site.[31] Interestingly, circular dichroism spectra indicate that $[Fe_4S_4]$ cluster nitrosylation decreases the $\varepsilon_{222}/\varepsilon_{208}$ ellipticity ratio from 1.199 ± 0.005 to 0.90 ± 0.04 from native to nitrosylated EndoIII (Figure 5), which is consistent with disordering of α helices.[53] Despite this disordering, $[Fe_4S_4]$ cluster nitrosylation does not appear to lower the DNA-binding affinity. Accordingly, the absence of DNA-bound redox activity of nitrosylated EndoIII cannot be explained by nitrosylated EndoIII having a significantly lower DNA-binding affinity than native EndoIII. Since the DNA-binding affinity of nitrosylated EndoIII is not lower than native EndoIII, we suspected that the reduction potential of nitrosylated EndoIII is no longer at 80 mV vs NHE.

Cluster Nitrosylation Shifts the EndoIII Reduction Potential by 800 mV in the Negative Direction.

Since redox activity of nitrosylated EndoIII is not observed on DNA-modified gold electrodes despite native and nitrosylated EndoIII having similar DNA-binding affinities, we turned to direct electrochemistry experiments in the absence of DNA on a graphite electrode with a wider potential window. Using differential pulse voltammetry, we observe a reduction potential of 127 ± 6 mV vs NHE in the voltammogram of native EndoIII (Figure 5). This value is consistent with previous measurements of EndoIII in the absence of DNA and is assigned as the $[Fe_4S_4]^{2+/3+}$ reduction potential.[41] However, the differential pulse voltammogram of nitrosylated EndoIII reveals a new reductive peak at −674 ± 8 mV vs NHE. The new reduction signal is specific to nitrosylated EndoIII and corresponds to an approximately 800 mV negative shift in reduction potential relative to native EndoIII. This shift places the reduction potential of nitrosylated EndoIII within a reasonable range to be reduced by dithionite (reduction potential range of −650 to −752 mV vs NHE from pH 6.9–7.9)[54] and also in the range of reduction potentials (−500 to −1000 mV vs NHE) measured for dinitrosyl iron and Roussin's red ester model complexes.[55–59] We are unable to assign the reduction potential of −674 mV vs NHE to either iron nitrosyl species specifically. However, considering that by EPR we observe the reduction of both the dinitrosyl iron complex and Roussin's red ester by dithionite, it is reasonable that the reductive wave at −674 mV vs NHE reflects the reduction of both iron nitrosyl species. Moreover, this reduction potential is outside the potential window of DNA-modified gold electrodes; the thiolated DNA and mercaptohexanol monolayer is compromised when sweeping potentials below −300 mV vs NHE (Figure S12). This shift in potential furthermore explains the lack of DNA-bound redox activity of nitrosylated EndoIII despite having a similar DNA-binding affinity to native EndoIII (Figure 5).

EndoIII Nitrosylation and Implications for DNA CT and NO Signaling.

Collectively, these data demonstrate that $[Fe_4S_4]$ cluster nitrosylation of the bacterial DNA repair enzyme EndoIII results in two distinct protein-bound iron nitrosyl complexes, the dinitrosyl iron complex and Roussin's red ester. The reaction of NO with EndoIII is similar in the absence and presence of DNA and leads to rapid and direct changes to the cluster with seemingly inconsequential changes in protein conformation. It is noteworthy that, despite this NO reactivity, the cluster in EndoIII is relatively stable to oxygen.

Importantly, unlike native EndoIII with an intact $[Fe_4S_4]$ cluster, nitrosylated EndoIII does not exhibit DNA-bound redox activity on DNA-modified gold electrodes. While there are conformational changes between native and nitrosylated EndoIII, nitrosylated EndoIII does not have a lower affinity for duplex DNA than native EndoIII. This observation is in contrast to NO-sensitive transcription factors in which $[Fe_4S_4]$ cluster nitrosylation modulates DNA-binding affinity as a result of a conformational change. Instead of changes to DNA-binding affinity, we observe an 800 mV decrease in reduction potential between native and nitrosylated EndoIII using direct electrochemical measurements. It therefore appears that the primary consequence of EndoIII $[Fe_4S_4]$ cluster nitrosylation is electrochemical in nature.

The results of this study have critical implications for the DNA CT model based on two primary observations: (1) native and nitrosylated EndoIII bind dsDNA to a similar extent and (2) nitrosylated EndoIII is more difficult to reduce than native EndoIII by 800 mV. These observations suggest that $[Fe_4S_4]$ cluster nitrosylation might affect DNA CT between nitrosylated and native DNA repair enzymes. Moreover, we observe that the presence of excess dsDNA does not inhibit cluster nitrosylation under our reaction conditions indicating that both free and DNA-bound EndoIII are susceptible to NO. Within the context of NO signaling, this study expands the known bioinorganic effects of NO. In contrast to transcription factor cluster nitrosylation for modulating DNA binding and gene expression, we observe that $[Fe_4S_4]$ cluster nitrosylation of a DNA repair enzyme results in a minimal change to DNA binding but a substantial modulation of redox activity.

Supplementary Material

Refer to Web version on PubMed Central for supplementary material.

ACKNOWLEDGMENTS

This work was supported by GM126904 from the National Institutes of Health (to J.K.B.). The Caltech EPR facility is supported by the National Science Foundation (NSF-1531940) and the Dow Next Generation Educator Fund. The Proteome Exploration Laboratory is supported by the Beckman Institute and the National Institutes of Health (1S10OD02001301). This research benefited from the use of the Autoflex MALDI TOF mass spectrometer in the Caltech CCE Multiuser Mass Spectrometry Laboratory, acquired with funds from the Dow Corporation. The authors thank Andy Zhou for assistance with protein overexpression and purification.

REFERENCES

(1.) Rees DD; Palmer RM; Moncada S Proc. Natl. Acad. Sci. U.S. A 1989, 86, 3375–3378. [PubMed: 2497467]

2.) Dimmeler S; Fleming I; Fisslthaler B; Hermann C; Busse R; Zeiher AM Nature 1999, 399, 601–605. [PubMed: 10376603]

3.) Zhou L; Zhu D-Y Nitric Oxide 2009, 20, 223–230. [PubMed: 19298861]

4.) Calabrese V; Mancuso C; Calvani M; Rizzarelli E; Butterfield DA; Giuffrida Stella AM Nat. Rev. Neurosci 2007, 8, 766–775. [PubMed: 17882254]

5.) Wink DA; Hanbauer I; Krishna MC; DeGraff W; Gamson J; Mitchell JB Proc. Natl. Acad. Sci. U. S. A 1993, 90, 9813–9817. [PubMed: 8234317]

6.) Kröncke K-D; Fehsel K; Kolb-Bachofen V Nitric Oxide 1997, 1, 107–120. [PubMed: 9701050]

7.) Fukumura D; Kashiwagi S; Jain RK Nat. Rev. Cancer 2006, 6, 521–534. [PubMed: 16794635]

8.) Burke AJ; Sullivan FJ; Giles FJ; Glynn SA Carcinogenesis 2013, 34, 503–512. [PubMed: 23354310]

9.) Ying L; Hofseth L Cancer Res 2007, 67, 1407–1410. [PubMed: 17308075]

10.) Ambs S; Merriam WG; Bennett WP; Felley-Bosco E; Ogunfusika MO; Oser SM; Klein S; Shields PG; Billiar TR; Harris CC Cancer Res 1998, 58, 334–341. [PubMed: 9443414]

11) (a). Arora DP; Hossain S; Xu Y; Boon EM Biochemistry 2015, 54, 3717–3728. [PubMed: 25996573] (b)Lahiri T; Luan B; Raleigh DP; Boon EM Biochemistry 2014, 53, 2126–2135. [PubMed: 24628400] (c)Plate L; Marletta MA Mol. Cell 2012, 46, 449–460. [PubMed: 22542454]

12) (a). Arnold WP; Mittal CK; Katsuki S; Murad F Proc. Natl. Acad. Sci. U. S. A 1977, 74, 3203–3207. [PubMed: 20623] (b)Ignarro LJ; Buga GM; Wood KS; Byrns RE; Chaudhuri G Proc. Natl. Acad. Sci. U. S. A 1987, 84, 9265–9269. [PubMed: 2827174] (c)Stone JR; Marletta MA Biochemistry 1994, 33, 5636–5640. [PubMed: 7910035]

13.) Nunoshiba T; deRojas-Walker T; Wishnok JS; Tannenbaum SR; Demple B Proc. Natl. Acad. Sci. U. S. A 1993, 90, 9993–9997. [PubMed: 8234347]

14.) Ding H; Demple B Proc. Natl. Acad. Sci. U. S. A 2000, 97, 5146–5150. [PubMed: 10805777]

15.) Crack JC; Munnoch J; Dodd EL; Knowles F; Al Bassam MM; Kamali S; Holland AA; Cramer SP; Hamilton CJ; Johnson MK; Thomson AJ; Hutchings MI; Le Brun NE J. Biol. Chem 2015, 290, 12689–12704. [PubMed: 25771538]

16.) Volbeda A; Dodd EL; Darnault C; Crack JC; Renoux O; Hutchings MI; Le Brun NE; Fontecilla-Camps JC Nat. Commun 2017, 8, 15052. [PubMed: 28425466]

17.) Crack JC; Green J; Thomson AJ; Le Brun NE Acc. Chem. Res 2014, 47, 3196–3205. [PubMed: 25262769]

18.) Lancaster JR; Hibbs JB, Jr. Proc. Natl. Acad. Sci. U. S. A 1990, 87, 1223–1227. [PubMed: 2153975]

19) (a). Foster MW; Cowan JA J. Am. Chem. Soc 1999, 121, 4093–4100.(b)Kennedy MC; Antholine WE; Beinert HJ Biol. Chem 1997, 272, 20340–20347.

20.) Harrop TC; Tonzetich ZJ; Reisner E; Lippard SJ J. Am. Chem. Soc 2008, 130, 15602–15610. [PubMed: 18939795]

21.) Roussin ML Ann. Chim. Phys 1858, 52, 285–303.

22.) Tonzetich ZJ; Wang H; Mitra D; Tinberg CE; Do LH; Jenney FE, Jr.; Adams MWW; Cramer SP; Lippard SJ J. Am. Chem. Soc 2010, 132, 6914–6916. [PubMed: 20429508]

23.) Tinberg CE; Tonzetich ZJ; Wang H; Do LH; Yoda Y; Cramer SP; Lippard SJ J. Am. Chem. Soc 2010, 132, 18168–18176. [PubMed: 21133361]

24.) Fitzpatrick J; Kalyvas H; Shearer J; Kim E Chem. Commun 2013, 49, 5550–5552.

25.) Crack JC; Smith LJ; Stapleton MR; Peck J; Watmough NJ; Buttner MJ; Buxton RS; Green J; Oganesyan VS; Thomson AJ; Le Brun NE J. Am. Chem. Soc 2011, 133, 1112–1121. [PubMed: 21182249]

26.) Serrano PN; Wang H; Crack JC; Prior C; Hutchings MI; Thomson AJ; Kamali S; Yoda Y; Zhao J; Hu MY; Alp EE; Oganesyan VS; Le Brun NE; Cramer SP Angew. Chem., Int. Ed 2016, 55, 14575–14579.

27.) Rogers PA; Eide L; Klungland A; Ding H DNA Repair 2003, 2, 809–817. [PubMed: 12826281]

28.) Ren B; Duan X; Ding HJ Biol. Chem 2009, 284, 4829–4835.

29) (a). Gorodetsky AA; Boal AK; Barton JK J. Am. Chem. Soc 2006, 128, 12082–12083. [PubMed: 16967954] (b)Boal AK; Yavin E; Lukianova OA; O'Shea VL; David SS; Barton JK Biochemistry 2005, 44, 8397–8407. [PubMed: 15938629]

30) (a). Sontz PA; Mui TP; Fuss JO; Tainer JA; Barton JK Proc. Natl. Acad. Sci. U. S. A 2012, 109, 1856–1861. [PubMed: 22308447] (b)Grodick MA; Segal HM; Zwang TJ; Barton JK J. Am. Chem. Soc 2014, 136, 6470–6478. [PubMed: 24738733] (c)Boal AK; Genereux JC; Sontz PA; Gralnick JA; Newman DK; Barton JK Proc. Natl. Acad. Sci. U. S. A 2009, 106, 15237–15242. [PubMed: 19720997]

31.) Tse ECM; Zwang TJ; Barton JK J. Am. Chem. Soc 2017, 139, 12784–12792. [PubMed: 28817778]

32.) Arnold AR; Grodick MA; Barton JK Cell Chemical Biology 2016, 23, 183–197. [PubMed: 26933744]

33.) Cunningham RP; Asahara H; Bank JF; Scholes CP; Salerno JC; Surerus K; Münck E; McCracken J; Peisach J; Emptage MH Biochemistry 1989, 28, 4450–4455. [PubMed: 2548577]

34.) Maragos CM; Morley D; Wink DA; Dunams TM; Saavedra JE; Hoffman A; Bove AA; Isaac L; Hrabie JA; Keefer LK J. Med. Chem 1991, 34, 3242–3247. [PubMed: 1956043]

35.) D'Autréaux B; Horner O; Oddou J-L; Jeandey C; Gambarelli S; Berthomieu C; Latour J-M; Michaud-Soret I J. Am. Chem. Soc 2004, 126, 6005–6016. [PubMed: 15137765]

36.) Herold S; Exner M; Nauser T Biochemistry 2001, 40, 3385–3395. [PubMed: 11258960]

37.) Stoll S; Schweiger AJ Magn. Reson 2006, 178, 42–55.

38.) Crack JC; Green J; Le Brun NE; Thomson AJ J. Biol. Chem 2006, 281, 18909–18913. [PubMed: 16717103]

39.) Slinker JD; Muren NB; Gorodetsky AA; Barton JK J. Am. Chem. Soc 2010, 132, 2769–2774. [PubMed: 20131780]
40.) Pheeney CG; Arnold AR; Grodick MA; Barton JK J. Am. Chem. Soc 2013, 135, 11869–11878. [PubMed: 23899026]
41.) Bartels PL; Zhou A; Arnold AR; Nuñez NN; Crespilho FN; David SS; Barton JK Langmuir 2017, 33, 2523–2530. [PubMed: 28219007]
42.) Lin Z-S; Lo F-C; Li C-H; Chen C-H; Huang W-N; Hsu I-J; Lee J-F; Horng J-C; Liaw W-F Inorg. Chem 2011, 50, 10417–10431. [PubMed: 21939194]
43.) Yeh S-W; Lin C-W; Li Y-W; Hsu I-J; Chen C-H; Jang L-Y; Lee J-F; Liaw W-F Inorg. Chem 2012, 51, 4076–4087. [PubMed: 22404753]
44.) Costanzo S; Menage S; Purrello R; Bonomo RP;Fontecave M Inorg. Chim. Acta 2001, 318, 1–7.
45.) Tsou C-C; Lu T-T; Liaw W-FJ Am. Chem. Soc 2007, 129, 12626–12627.
46.) Enemark JH; Feltham RD Coord. Chem. Rev 1974, 13, 339–406.
47.) Cutsail GE, III.; Telser J; Hoffman BM Biochim. Biophys. Acta, Mol. Cell Res 2015, 1853, 1370–1394.
48.) Rhine MA; Sanders BC; Patra AK; Harrop TC Inorg. Chem 2015, 54, 9351–9366. [PubMed: 26086436]
49.) Ye S; Neese FJ Am. Chem. Soc 2010, 132, 3646–3647.
50.) Crack JC; Hamilton CJ; Le Brun NE Chem. Commun 2018, 54, 5992–5995.
51.) Radi R Proc. Natl. Acad. Sci. U. S. A 2004, 101, 4003–4008. [PubMed: 15020765]
52.) Purification of nitrosylated EndoIII by size-exclusion filtration removes, among other small-molecule reactants and products, labile Fe released by EndoIII [Fe_4S_4] cluster nitrosylation. If size-exclusion purification is omitted and EndoIII nitrosylation is instead performed directly on the electrode surface, increased redox activity is observed. This observation indicates that EndoIII cluster nitrosylation liberates labile Fe that overwhelms the surface passivation provided by mercaptohexanol and thiol-modified dsDNA. Moreover, this observation is consistent with the retention of three protein-bound Fe and liberation of one Fe as indicated by ratiometric EPR spin integration and the ferene assay.
53.) McNamara C; Zinkernagel AS; Macheboeuf P; Cunningham MW; Nizet V; Ghosh P Science 2008, 319, 1405–1408. [PubMed: 18323455]
54.) Mayhew SG Eur. J. Biochem 1978, 85, 535–547. [PubMed: 648533]
55.) Tsai F-T; Chiou S-J; Tsai M-C; Tsai M-L; Huang H-W; Chiang M-H; Liaw W-F Inorg. Chem 2005, 44, 5872–5881. [PubMed: 16060642]
56.) Hsieh C-H; Brothers SM; Reibenspies JH; Hall MB; Popescu CV; Darensbourg MY Inorg. Chem 2013, 52, 2119–2124. [PubMed: 23373599]
57.) Yeh S-W; Lin C-W; Liu B-H; Tsou C-C; Tsai M-L; Liaw W-F Chem. - Eur. J 2015, 21, 16035–16046. [PubMed: 26403796]
58.) Wang R; Camacho-Fernandez MA; Xu W; Zhang J; Li L Dalton Trans 2009, 777–786. [PubMed: 19156270]
59.) Sanina NA; Krivenko AG; Manzhos RA; Emel'yanova NS; Kozub GI; Korchagin DV; Shilov GV; Kondrat'eva TA; Ovanesyan NS; Aldoshin SM New J. Chem 2014, 38, 292–301.

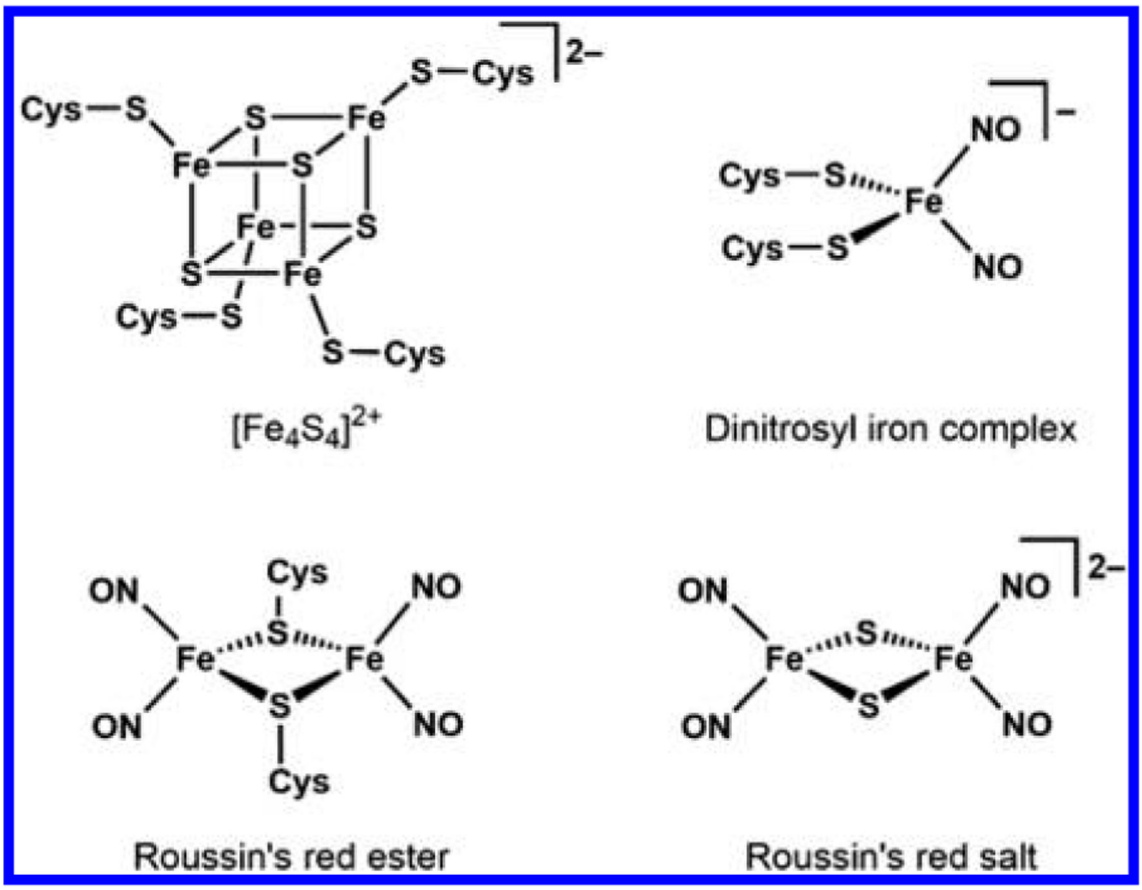

Figure 1.
Structure of a protein-bound $[Fe_4S_4]^{2+}$ cluster, dinitrosyl iron complex, Roussin's red ester, and the Roussin's red salt anion.

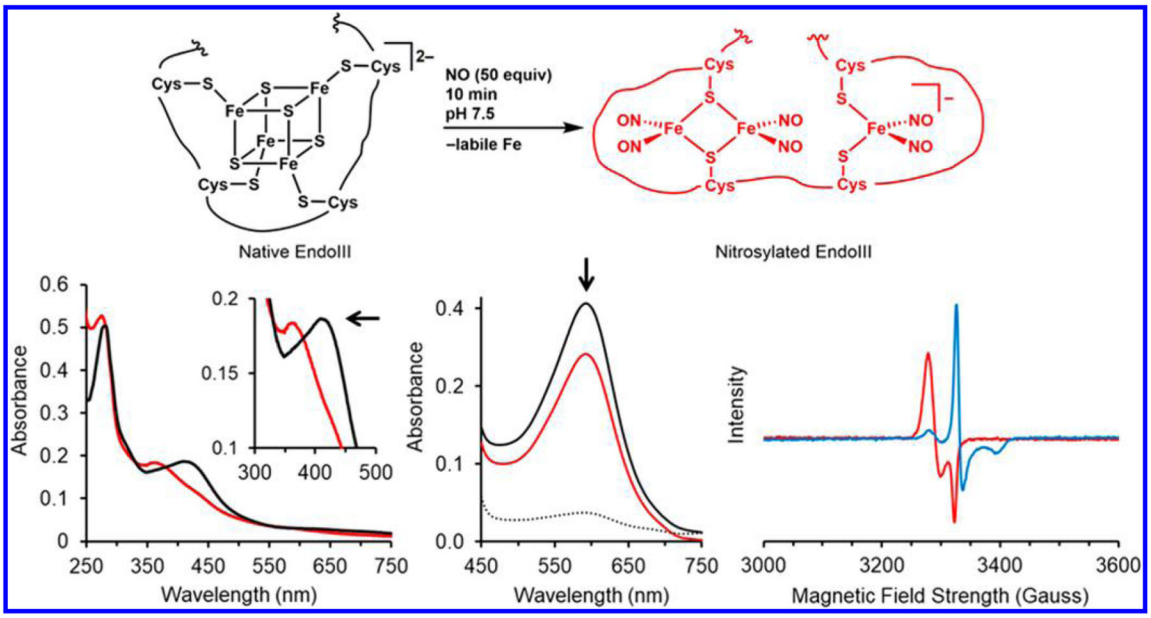

Figure 2.

Spectroscopic characterization of EndoIII [Fe_4S_4] cluster nitrosylation. (Top) Representation of the conversion of native EndoIII into nitrosylated EndoIII by a 10 min exposure to NO (50 equiv). (Bottom left) UV−vis spectra of native (black) and nitrosylated (red) EndoIII revealing a 46 nm hypsochromic shift (inset). (Bottom middle) Representative results of the ferene colorimetric assay for native EndoIII (black), nitrosylated EndoIII (red), and a buffer blank (dotted line). Native EndoIII contains 4.00 ± 0.09 Fe per cluster, and this value decreased to 3.05 ±0.01 Fe for nitrosylated EndoIII. (Bottom right) CW EPR spectra of nitrosylated EndoIII before (red) and after (blue) a 30 min treatment with sodium dithionite (25 equiv) recorded at 60 K, microwave frequency of 9.3701 GHz, and microwave power of 0.204 mW. All experiments were performed in the absence of DNA and buffer was pH 7.5 and contained 20 mM phosphates, 150 mM NaCl, 0.5 mM EDTA, and 10% v/v glycerol.

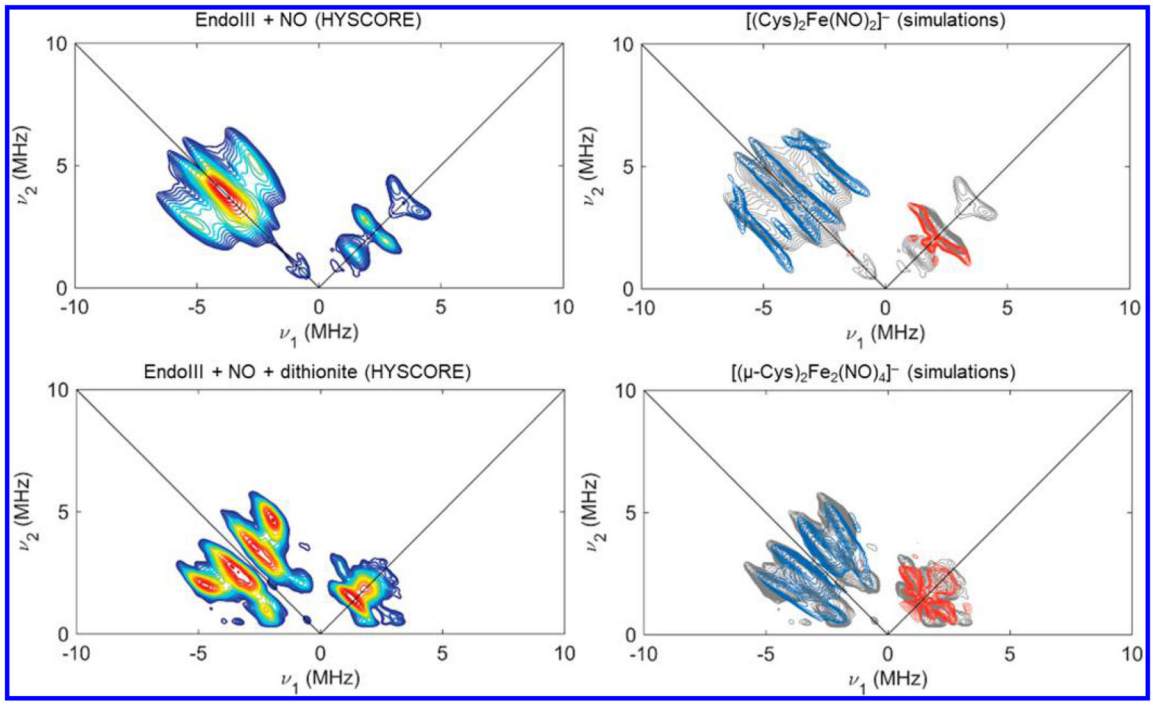

Figure 3.

X-band HYSCORE spectra and simulations of ^{14}N hyperfine couplings. (Top left) X-band HYSCORE spectrum of nitrosylated EndoIII acquired at 341.8 mT (g = 2.036) corresponding to the $[(Cys)_2Fe(NO)_2]^-$ dinitrosyl iron complex. (Bottom left) nitrosylated EndoIII after treatment with dithionite acquired at 348.5 mT (g = 1.998) corresponding to the $[(\mu\text{-}Cys)_2Fe_2(NO)_4]^-$ reduced Roussin's red ester. Left panels show the experimental spectra, with intensities indicated by colors ranging from blue to red in order of increasing intensity. The rightmost panels depict the experimental data in gray and overlay simulations from a relatively strongly coupled ^{14}N nucleus (blue, denoted N_1) and a relatively weakly coupled ^{14}N nucleus (red, denoted N_2). Specific simulation parameters are detailed in Table 1. Acquisition parameters: temperature = 20 K; microwave frequency = 9.740 GHz (a), 9.744 GHz (b); MW pulse lengths $\pi/2$, π = 8, 16 ns; τ = 138 ns (a), 138 ns (b); $t_1 = t_2$ = 100 ns; $\Delta t_1 = \Delta t_2$ = 16 ns; shot repetition time (srt) = 1 ms.

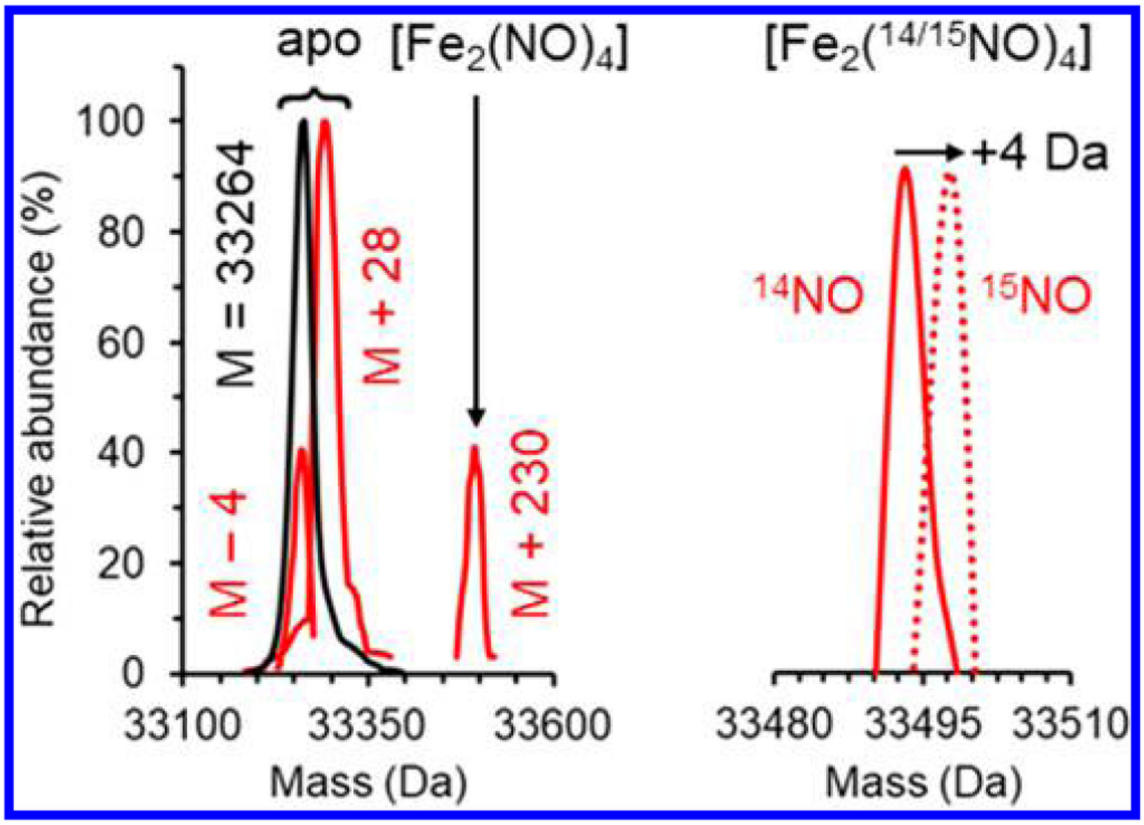

Figure 4.

Deconvoluted mass spectra of (left) native (black) and nitrosylated (red) EndoIII and (right) nitrosylated EndoIII prepared using ^{14}NO (solid) and ^{15}NO (dotted).

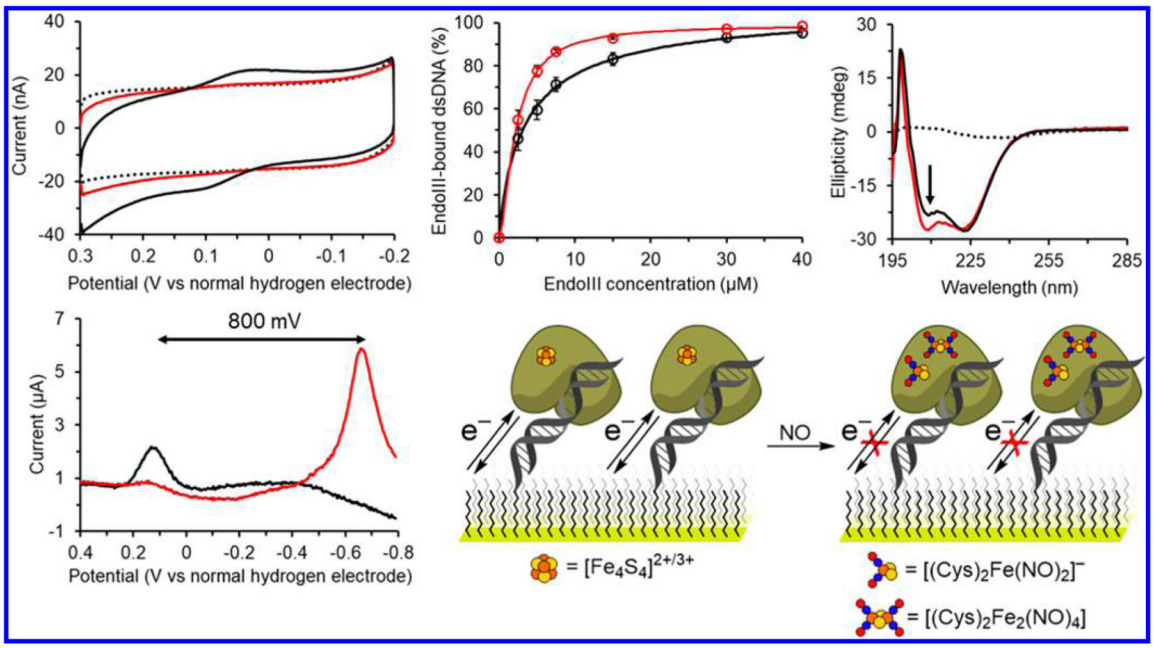

Figure 5.

Biophysical and electrochemical characterization of native and nitrosylated EndoIII. (Top left) Cyclic voltammograms of buffer (dotted), native EndoIII (black), and nitrosylated EndoIII (red) on a DNA-modified gold electrode. (Top middle) Results of electrophoretic mobility shift assays plotted as EndoIII-bound dsDNA as a function of EndoIII concentration. Open circles and error bars represent the mean and standard error ($n = 5$), respectively. Solid lines represent Hill function fitting used to calculate dissociation constants. (Top right) Circular dichroism spectra of buffer (dotted), native EndoIII (black), and nitrosylated (red) EndoIII. (Bottom left) Differential pulse voltammograms of background-subtracted native (black) and nitrosylated (red) EndoIII on an edge-plane graphite electrode. Samples used in circular dichroism and graphite electrochemistry experiments did not contain DNA. (Bottom right) Representation of a DNA-modified gold electrode surface with native EndoIII (left) and nitrosylated EndoIII (right). Small black lines represent mercaptohexanol used to passivate the gold electrode surface. DNA-bound redox activity is not observed for nitrosylated EndoIII despite having a similar DNA-binding affinity to native EndoIII.

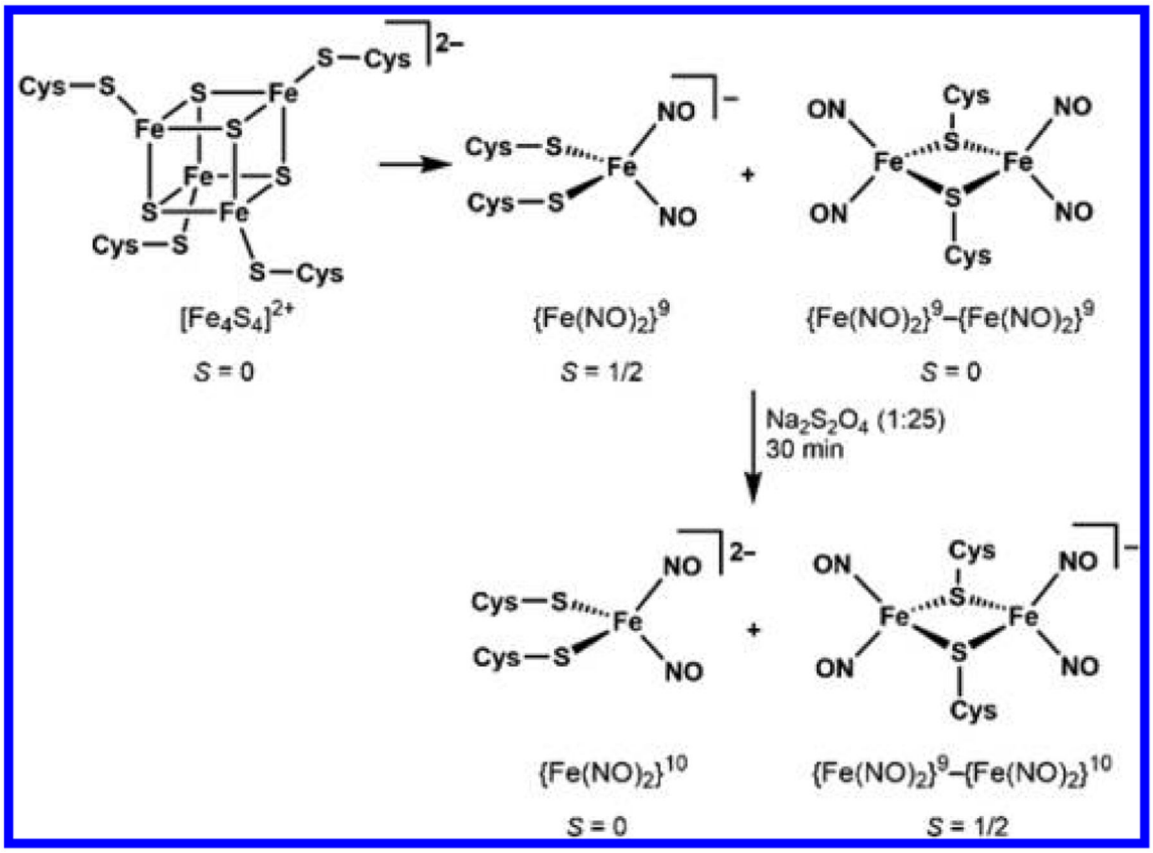

Scheme 1.

Cluster Nitrosylation Followed by Reduction by Dithionite As Visualized through Conversions between EPR-Active and EPR-Silent States

Table 1.

Combined ^{14}N Hyperfine and Nuclear Quadrupole Coupling Parameters for EPR-Active Nitrosylated Species Observed in EndoIII

species	nucleus	A (MHs)	a_{iso} [a] (MHz)	$(\alpha,\beta,\gamma)_{HFC}$°	e^2qQ/h (MHz)	η	$(\alpha,\beta,\gamma)_{NQI}$°
$[(Cys)_2Fe(NO)_2]^-$	$^{14}N_1$	[17.1,4.3, 7.1]	9.5	(0, 0, 0)	1.4	>0.1	(0, 0, 0)
g = [2.042, 2.036, 2.015]	$^{14}N_2$	[−1.6, −1.6, 4.3]	0.4	(0, −30, 0)	0.8	>0.1	(0, −30, 0)
$[(\mu\text{-Cys})_2Fe_2(NO)_4]^-$	$^{14}N_1$	[1.4, 8.9, 1.4]	3.9	(0, 0, 0)	1.2	>0.2	(0, 0, 0)
g = [2.011, 2.010, 1.972]	$^{14}N_2$	[−1.4, 3.2, 3.9]	1.9	(0, 0, 0)	1.0	>0.1	(0, 0, 0)

[a] Isotropic hyperfine coupling constant, defined as $a_{iso} = (A_1 + A_2 + A_3)/3$.